



HAL
open science

(SI) The Energetics of Inorganic Nanotubes.

Mark Wilson, Clare Bishop

► **To cite this version:**

Mark Wilson, Clare Bishop. (SI) The Energetics of Inorganic Nanotubes.. Molecular Physics, 2008, 106 (12-13), pp.1665-1674. 10.1080/00268970802304593 . hal-00513220

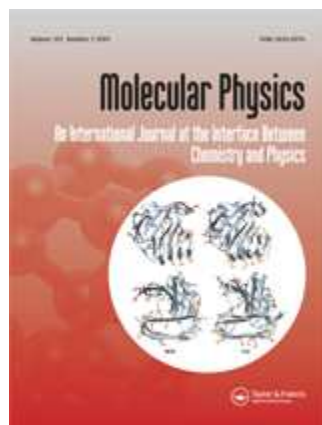
HAL Id: hal-00513220

<https://hal.science/hal-00513220>

Submitted on 1 Sep 2010

HAL is a multi-disciplinary open access archive for the deposit and dissemination of scientific research documents, whether they are published or not. The documents may come from teaching and research institutions in France or abroad, or from public or private research centers.

L'archive ouverte pluridisciplinaire **HAL**, est destinée au dépôt et à la diffusion de documents scientifiques de niveau recherche, publiés ou non, émanant des établissements d'enseignement et de recherche français ou étrangers, des laboratoires publics ou privés.



(SI) The Energetics of Inorganic Nanotubes.

Journal:	<i>Molecular Physics</i>
Manuscript ID:	TMPH-2008-0107.R1
Manuscript Type:	Full Paper
Date Submitted by the Author:	17-Jun-2008
Complete List of Authors:	Wilson, Mark; University of Oxford, Physical and Theoretical Chemistry Bishop, Clare; University College London, Chemistry
Keywords:	Inorganic nanotubes, Computer simulation, Carbon nanotubes
<p>Note: The following files were submitted by the author for peer review, but cannot be converted to PDF. You must view these files (e.g. movies) online.</p> <p>swnt_energetics_postref.tex</p>	



Molecular Physics
The Energetics of Inorganic Nanotubes.

Clare L. Bishop[†] and Mark Wilson*.

[†]*Department of Chemistry, University College London, 20 Gordon Street, London WC1H 0AJ,
U.K.*

^{*}*Department of Chemistry, Physical and Theoretical Chemistry Laboratory, University of Oxford,
South Parks Road, Oxford OX1 3QZ, U.K.*

Abstract

The energetics of inorganic nanotubes (INTs) are investigated using both atomistic and continuum models. A relatively simple (Tersoff-II) potential model is used to study the energetics of carbon nanotube (C-NT) formation for use as a well-understood reference system. INTs formed by folding sections of MX stoichiometry constructed from both percolating hexagonal and square-net sheets are modelled. The C-NTs and hexagonal INTs are found to display folding energetics essentially consistent with a continuum elastic model. The square net INTs are found to display folding energetics which are strongly dependent upon the direction along which the originating sheet is folded (and hence on the morphology of the formed INT). The difference in energies as a function of INT morphology is exemplified by reference to the high symmetry cases [the $(n, 0)_{sq}$ and $(n, n)_{sq}$ INTs] which are discussed in terms of the detailed atomistic interactions.

Typeset using REVTeX

1
2
3
4
5
6
7
8
9
10
11
12
13
14
15
16
17
18
19
20
21
22
23
24
25
26
27
28
29
30
31
32
33
34
35
36
37
38
The discovery of carbon fullerenes [1] and the subsequent observation of related carbon nanotubes [2–4] indicates that the traditional views of phase diagrams may require re-evaluation for even apparently simple elements. Since these observations, there has been significant interest in the potential stability of analogous low-dimensional ordered (crystalline) structures. The experimental observation of these low dimensional structures can be broadly split into two classes. Nanotubular (inorganic nanotube - INT) structures can be isolated for systems such as MoS₂, WS₂ [5] and NiCl₂ [6], generated both by physical (electron-beam irradiation, laser ablation and arc-discharge) and chemical methods (in gas-phase reactors) [5]. The structure of these INTs can be related to the bulk “layered” crystal structures in a direct analogue to the formation of carbon nanotubes from a single graphene sheet. In addition, INTs have been produced for systems as diverse as BN and BN/C [7], TiO₂ [8] and CdS/CdSe [9] (see ref. [10] for a recent review and more exhaustive list). Alternatively, high resolution transmission electron microscopy studies show how low-dimensional structures may form by filling carbon nanotubes [11,12] from molten salts (for example, NiO, PbO, Bi₂O₃, V₂O₅ and MoO₃ [11,13–16], UCl₄ [17], AgCl/AgBr [18,19], KI [20,21], BaI₂ [22], CoI₂ [23] and Sb₂O₃ [24]). In addition, the existence of other INT structures (*i.e.* GaN [25], GaSe [26] and elemental phosphorous [27]) has been predicted theoretically.

39
40
41
42
43
44
45
46
47
48
49
50
51
52
53
54
55
56
57
58
59
60
For simple ionic salts such as KI, the stability of nanotubular structures can be understood by reference to relatively simple ion-based simulation models [28–33] and by higher level electronic structure calculations [34]. Furthermore, these models can then be used in a predictive mode in order to identify possible new structures for experimental investigation. Recent work, for example, has demonstrated the stability of a novel classes of INTs whose structures may be understood in terms of the folding of sheets of both square- and hexagonal-nets [28–33]. The clear implication is that such nanotubular structures may be ubiquitous, forming a metastable phase diagram which maps onto the (thermodynamic)

equilibrium phase diagram. A central question, therefore, concerns how to access these metastable phase diagrams and hence control the final INT morphologies. Such control is critical if potentially useful physical and electronic properties are to be fully exploited. For example, bulk semiconductors such as CdS and CdSe would be expected to form INTs in which the band gaps were morphology-dependent. A key property to be investigated, therefore, are the energetics of formation. The energetics of the single-walled carbon nanotubes (SWCNTs) appear to follow a relatively simple dependence (see ref. [35] and references therein). However, it is not clear that this simple diameter dependence should transfer to other nanotubular structures, in particular those in which coulombic interactions may be significant. An understanding of the factors which control these energetics is critical if the INTs are to be manufactured in a controlled fashion.

In this Paper we consider the energies of a range of nanotubular structures formed from both hexagonal sheets and square plain nets. Our goal is to understand the factors which control these energetics and, as a result, progress towards the formation of longer length-scale (mesoscopic) models. Two approaches are considered in order to augment the relatively well-developed atomistic models. Firstly, the INT energies are considered in terms of the energy required to fold the sheets into cylinders and compared to elastic continuum predictions. Secondly, the atomistic energies are deconstructed in terms of the interactions of chains of percolating anion-cation linkages in a manner analogous to that described by Bichoutskaia and Pyper [36]. The Paper is arranged as follows. The folding of the square and hexagonal nets is described in section II. Section III describes the details of the atomistic potential models. In section IV the details of the continuum elastic model, and its comparison to the atomistic model results, are explored. In section V an analytic atomistic model is developed and the results compared to both the atomistic potential model and continuum elastic model results.

In addition to the well-documented carbon nanotubes, in this paper we shall also consider the two classes of INT illustrated in figure 1. The structures of these two classes can be understood in terms of folding two dimensional sheets of percolating hexagons and squares respectively. In both cases the unit cells contain two atoms (corresponding to one MX stoichiometric unit). The folding of the hexagonal sheets are analogous to the folding of the graphene sheet to form the carbon nanotubes, with the exception that the two atoms in the unit cell have different chemical identities. In both cases INTs are generated by selecting a chiral vector, $\mathbf{C}_h = (n\mathbf{a}_1 + m\mathbf{a}_2)$, where \mathbf{a}_1 and \mathbf{a}_2 are the respective unit cell vectors. As a result, pairs of integers (n, m) can be used to define the final INT morphology. In order to distinguish between the INTs formed from the hexagonal and square plain sheets, we employ a nomenclature of the form $(n, m)_{hex}$ and $(n, m)_{sq}$ respectively.

III. POTENTIAL MODELS.

The carbon potential chosen for this study is a three-body (Tersoff II) model [38]. This model reproduces the basic bulk structural and energetic properties, whilst retaining a relatively simple functional form. The relatively simple form allows it to be readily incorporated with the ionic potentials to allow for the direct observation of C-NT filling in which the enclosing carbon tube is treated as flexible [37].

The ion-ion interactions are accounted for using a rigid ion pair-wise additive Born-Mayer potential,

$$U(r_{ij}) = B_{ij}e^{-a_{ij}r_{ij}} + \frac{Q_i Q_j}{r_{ij}} - \frac{C_6^{ij}}{r_{ij}^6}, \quad (3.1)$$

where B_{ij} and a_{ij} are parameters representing the contribution of the ion radii to the repulsive wall and the rate of decay of the repulsion respectively, C_6^{ij} are the dipole-dipole dispersion parameters and $Q_{i(j)}$ is the (formal) charge on ion $i(j)$. The long-range electrostatic interactions are accounted for using an Ewald summation. In the present work two

basic potential models are considered which differ simply in terms of the short-range parameters (and hence favour different bulk crystal structures). The first parameter set (termed potential I hereafter) thermodynamically favours the wurtzite (B4, four-coordinate ions) over the rocksalt (B1, six-coordinate ions) whilst for the second parameter set (potential II) the two crystal structures have equal energies (and different volumes) at their respective minima. The potential parameters are listed in table I.

IV. FOLDING MODEL.

If the two-dimensional structures (figure 1) behave as simple macroscopic sheets then an elastic continuum model suggests a relationship between the INT energy and the radius of the form [39,40]

$$E_{\sigma} = \frac{\pi E T h^3}{12R}, \quad (4.1)$$

where E is the elastic modulus of the sheet, h is the thickness of the sheet being folded, T is the length of the final folded tube and R is the radius of the formed INT. T can be linked to the area of the folded tube by $A = 2\pi RT$ and so,

$$E_{\sigma} = \frac{E h^3 A}{24R^2}. \quad (4.2)$$

For a INT generated from folded hexagons, the unit cell (which contains two atoms) has area $A_{uc} = \frac{\sqrt{3}}{2}a^2$, giving the total area of the INT as $A = N A_{uc}$, where N is the number of unit cells making up the INT. As a result, for a hexagon-based INT

$$\frac{E_{\sigma}}{N} = \frac{\sqrt{3} E h^3 a^2}{48R^2}, \quad (4.3)$$

whilst for a square-based INT (where $A_{uc} = a^2$)

$$\frac{E_{\sigma}}{N} = \frac{E h^3 a^2}{24R^2}. \quad (4.4)$$

Alternatively, these may be expressed simply as,

$$\frac{E_{\sigma}}{N} = \frac{F}{R^2}, \quad (4.5)$$

which allows for a more direct comparison between systems as a somewhat arbitrary value of the sheet thickness (h) does not have to be selected. Figure 2 shows the energies of a range of single-walled CNTs of differing morphologies displayed relative to the energy of an infinite graphene sheet. **Each successive curve in the main body of the figure represents the energy of a nanotube of a specified morphology as a function of the radius of that CNT. In each case an effective infinite CNT is modelled by constructing a simulation cell so as to contain an integral number of unit cells and employing periodic boundary conditions. The (n, n) and $(n, 0)$ CNTs simulation cells contain 20 and 12 unit cells respectively (corresponding to simulation cells of the order to 50Å in length). The simulation cell length at each radius is varied in order to determine the energy minimum at that radius. As a result, reach minima represents the energy as a function of INT radius for a fully relaxed nanotube of given morphology.** The energies are shown plotted against the radii of the fully relaxed carbon nanotubes. The figure inset also shows the fit of the respective energy minima to a R^{-n} polynomial, showing that, for this model, $n \simeq 2$ which is consistent with an elastic continuum model. The carbon nanotubes energetics, modelled with the Tersoff-II potential, appear to follow simple continuum behaviour and, as a result, their energetics appears to depend most significantly on their radii and only subtly their detailed morphology. The limited number of nanotubes of morphology other than $(n, 0)$ and (n, n) studied (here the $(3, 1)$, $(3, 2)$, $(4, 1)$ and $(5, 3)$ C-NTs **studied using repeating simulation cells containing 4, 4 , 10 and 2 unit cells respectively**) further support this observation. Use of equation 4.3 requires the definition of a sheet thickness (h) in order to determine the elastic modulus (usually chosen as the nearest-neighbour layer-layer separation in graphite, giving $h = 3.4\text{\AA}$). However, as our focus here is on a range of INTs, we shall quote values for the collection of parameters, F . The present work gives values of $F = 1.62\text{eV}\text{\AA}^{-2}$ and $F = 1.57\text{eV}\text{\AA}^{-2}$ for the $(n, 0)$ and (n, n) C-NTs respectively.

These compare with DFT-derived values of between $2.0\text{eV}\text{\AA}^{-2}$ for a range of (n, n) tubes and $2.15\text{eV}\text{\AA}^{-2}$ and $2.16\text{eV}\text{\AA}^{-2}$ for the $(8, 4)$ and $(10, 0)$ nanotubes respectively [41]. We note that detailed high level DFT calculations indicate a subtle dependence of the folding energies on the C-NT morphology [42].

Figure 3 shows the energies of the hexagonal INT structures, constructed for both $(n, 0)_{hex}$ and $(n, n)_{hex}$ morphologies, again as a function of the INT radii, displayed relative to the energy of the infinite hexagonal sheet. As for figure 2, successive curves show the energies of each INT (or specific morphology) as a function of radius with the energy minimum representing the fully relaxed energy and radius for that specific INT. Again, effectively infinite INTs are constructed by applying periodic boundary conditions in which the central simulation cell contains four and seven unit cells for the $(n, 0)_{hex}$ and $(n, n)_{hex}$ morphologies respectively. The energies shown are obtained using both potentials I and II. Again, as highlighted by the fit to a polynomial of the form R^{-n} (shown in the inset to the figure), the value of $n \simeq 2$ indicates that these systems appear to behave as an elastic continuum. The F -values are 0.73 and $0.62\text{eV}\text{\AA}^{-2}$ for the $(n, 0)_{hex}$ and $(n, n)_{hex}$ INTs with potential I, and 0.73 and $0.60\text{eV}\text{\AA}^{-2}$ for the corresponding INTs using potential II. The relative invariance of these values to the details of the atomistic potential model indicates that it may be the coulombic interactions which are dominating these properties.

Figure 4a shows the energies of the square-based INT structures, over a range of morphologies, as a function of their radii, displayed relative to the energy of an infinite square plain sheet. As for figures 2 and 3 each curve represents the energy as a function of the radius for a tube of specified morphology, in these cases calculated for repeating simulation cells containing five unit cells. In contrast to either the carbon (figure 2) and hexagonal INTs (figure 3) the energetics of these structures appear to show a strong dependence on their morphology, coupled with the clear dependence on radius. In order to understand these energies we shall initially focus on the $(n, 0)_{sq}$ and $(n, n)_{sq}$ INT

morphologies. Figure 4b shows the energetics of these two INT morphologies as a ln-ln plot in order to highlight any simple polynomial dependence on the INT radius. The $(n, 0)_{sq}$ INTs appear to follow the R^{-2} dependence associated with the elastic continuum, whilst the $(n, n)_{sq}$ INTs appear to show a more complex radius-dependence, with best fit polynomial orders of $n \sim 2.9$ and $n \sim 3.4$ for potentials I and II respectively. As a result, we are able to determine an elastic modulus-related F -value for the $(n, 0)_{sq}$ INTs of 1.42 and $1.51 \text{eV}\text{\AA}^{-2}$.

Table II compares the elastic moduli-related F -values (equation 4.5) for the systems showing the R^{-2} continuum elastic model energetic dependence of the INT radius. Overall, therefore, both the hexagonal- and square-net-based $(n, 0)_{sq}$ INTs are easier to fold (smaller F) than the C-NTs of corresponding radius. The square-net-based INTs are more difficult to form than the corresponding hexagonal sheets.

V. CHAIN MODEL.

A. $(n, n)_{sq}$ INTs.

In order to understand the relative energetics of the $(n, 0)_{sq}$ and $(n, n)_{sq}$ INTs, it is clear that we need to go beyond an elastic continuum model and involve the atomistic detail of their structures. Our starting point for this analysis is the work of Bichoutskaia and Pyper [36]. These authors consider the energetics of pseudo-one-dimensional crystal structures which are directly related to an underlying bulk rocksalt structure. The natural starting point is to consider an infinite square-net plain (figure 1), for which the electrostatic (coulombic) energy may be expressed as

$$U^{coul}(a, b) = -\frac{2\ln 2}{b} + U^{ic}(a, b), \quad (5.1)$$

where a and b are the nearest-neighbour anion-cation separations parallel to and perpendicular to a chosen vector linking a nearest-neighbour anion-cation pair and which is chosen to correspond to the final INT major axis. In equation 5.1 the first term represents the sum of the ionic interactions in a single linear chain (for which the Madelung constant is $2\ln 2$)

whilst the second term represents the inter-chain (*ic*) interaction of a given chain with all other chains. Following Bichoutskaia and Pyper, the inter-chain energy may be written as

$$U^{ic}(a, b) = 2 \sum_{i=1}^{\infty} \left\{ \frac{(-1)^i}{ia} + 2 \sum_{j=1}^{\infty} \left[\frac{(-1)^{i+j}}{(i^2a^2 + j^2b^2)^{1/2}} \right] \right\}, \quad (5.2)$$

where i and j are indices labelling ions parallel and perpendicular to the major axis (the 'b' direction). Alternatively, taking $x = a/b$ (the ratio of the nearest-neighbour anion-cation separations parallel to and perpendicular to the final INT major axis),

$$\begin{aligned} U^{ic}(b, x) &= 2 \sum_{i=1}^{\infty} \left\{ \frac{(-1)^i}{ibx} + 2 \sum_{j=1}^{\infty} \left[\frac{(-1)^{i+j}}{b(i^2x^2 + j^2)^{1/2}} \right] \right\}, \\ &= \frac{2}{b} \sum_{i=1}^{\infty} \left\{ \frac{(-1)^i}{ix} + 2 \sum_{j=1}^{\infty} \left[\frac{(-1)^{i+j}}{(i^2x^2 + j^2)^{1/2}} \right] \right\}. \end{aligned} \quad (5.3)$$

The total energy of the planar structure is given by

$$U^{tot}(b, x) = U^{ic}(b, x) - \frac{2 \ln 2}{b} + U^{sr}(b, x), \quad (5.4)$$

where $U^{sr}(b, x)$ is the short-range energy. Assuming only the nearest-neighbour anion-cation interactions to be significant, and neglecting dispersion terms, then the Born-Mayer potential gives

$$U^{sr}(b, x) = 2B_{+-}e^{-ab} + 2B_{+-}e^{-abx}. \quad (5.5)$$

The above equations for the interaction energy can be readily modified to deal with an $(n, n)_{sq}$ INT. In these cases the interaction energy becomes

$$U_{(n,n)}^{ic}(b, x) = \frac{1}{b} \sum_{i=1}^{2n} \left\{ \frac{(-1)^i}{L_i x} + 2 \sum_{j=1}^{\infty} \left[\frac{(-1)^{i+j}}{(K_i^2 x^2 + j^2)^{1/2}} \right] \right\}, \quad (5.6)$$

where

$$L_i = \frac{\sin\left(\frac{i\pi}{2n}\right)}{\sin\left(\frac{\pi}{2n}\right)}, \quad (5.7)$$

is a geometric factor that accounts for the folding of the square plain (see **Appendix I**).

The replacement of a sum to infinity with a sum to $2n$ reflects the change from considering

an infinite sheet to a finite folded sheet. The $2n$ limit also reflects the presence of two anion-cation chains per unit cell (which run at an angle of 45° to both \mathbf{a}_1 and \mathbf{a}_2).

Figure 5a shows the $(n, n)_{sq}$ INT energy as a function of the parameter n for key values of the INT dimensions b and x . Each point represents the optimal energy of an INT (displayed with respect to the energy of the infinite unfolded sheet) with the structure relaxed with respect to the constraints listed below. These are:

- b is fixed to the value obtained from the energy minimisation of the infinite square plain ($b = 4.070\text{au}$ for potential I and $b = 4.620\text{au}$ for potential II and $a = b$ ($x = 1$)).
- b fixed at the infinite square plain values, with x allowed to relax at each n .
- Both b and x are allowed to fully relax at each n .

In all cases b and x are obtained by finding the energy minima numerically. Figure 5a highlights the effect of successive relaxations, with the relaxation of x appearing more energetically significant than the relaxation of b alone. Figure 5b shows the relaxed geometric factor, x , as a function of the n -index for the $(n, n)_{sq}$ INTs. For the small INTs x is greater than one, as observed experimentally [20]. The corresponding geometric parameters obtained by Bichoutskaia and Pyper are shown for comparison. The sections considered are $(2 \times 2 \times \infty)$, $(3 \times 3 \times \infty)$ and $(4 \times 4 \times \infty)$, where $(m \times m \times \infty)$, refers to the number of ions along each side of the square cross-section perpendicular to the major crystallite axis. To allow for a direct comparison with the present work, these values are plotted with the number of molecules per square plain along the x -axis. The multiple values for each crystallite reflect changes in the repulsive wall hardness expressed in terms of polynomial A/r^m , where $m = \{6, 9, 10.5, 12\}$ which acts to control the INT geometry. The use of an exponential potential in the current work has an analogous effect. For example, further increasing the short-range parameter B_{MX} (*i.e.* effectively increasing the cation radius) has the effect of further damping the relaxed a/b ratio.

Equation 5.6 can be used to define an effective Madelung constant,

$$M_b(x) = -2\ln 2 + \sum_{i=1}^{2n} \left\{ \frac{(-1)^i}{K_i x} + 2 \sum_{j=1}^{\infty} \left[\frac{(-1)^{i+j}}{(K_i^2 x^2 + j^2)^{1/2}} \right] \right\}. \quad (5.8)$$

Figure 6 shows the value of the M_b as a function of the index n . The Madelung constant highlights the effect of relaxing both b and x more dramatically than considering the bare energetics. The $(n, n)_{sq}$ Madelung constants rapidly tend to the two dimension square planar limit ($M_b = -1.618$) as n increases. For comparison, the figure also shows the Madelung constants from reference [36] calculated for sections of the bulk rocksalt crystal structure. Again, these values are plotted against the number of molecules in a square cross-section perpendicular to the crystallite major axis. As would be expected, the bulk-like structures show Madelung constants which tend towards the bulk rocksalt limit ($M_b = -1.7476$). As would be expected, the $(3 \times 3 \times \infty)$ crystallite becomes energetically favourable with respect to a nanotube of comparable density (number of ions per unit length) reflecting the presence of fully coordinated ions in the former crystallite. However, these energies refer to the *free* (unenclosed by a C-NT) crystallites. In the confined (cylindrical) environments afforded by the C-NTs the INT-like structures would be expected to be energetically favoured, at least for relatively small diameter structures. We note that, for example, mass spectrometry experiments [43] coupled with potential model calculations [44] indicate the presence of $(\text{MgO})_n$ clusters constructed from percolating $(\text{MgO})_3$ hexagons [or $(3, 3)_{sq}$ INTs in the present notation].

B. $(n, 0)_{sq}$ INTs.

An analogous set of equations can be derived to account for the interactions in the $(n, 0)_{sq}$ INTs. The anion-cation chain energy is modified to become,

$$U_{(n,0)}^{chain} = -\frac{2}{b} \sum_{m=1}^{m=\infty} \frac{(-1)^{m+1}}{[(D_{\perp}^m)^2 + (D_{\parallel}^m)^2]^{\frac{1}{2}}}, \quad (5.9)$$

where D_{\parallel}^m and D_{\perp}^m are the components parallel and perpendicular to the final formed INT major axis, that is,

$$D_{\parallel}^m = \frac{m\sqrt{2}}{2}, \quad (5.10)$$

$$D_{\perp}^m = \frac{\sqrt{2}n}{\pi} \sin\left(\frac{m\pi}{2n}\right). \quad (5.11)$$

Again, the INT is considered as constructed from n chains (labelled q [$q = 1, 2, \dots, n-1, n$]),

$$U_{(n,0)}^{ic} = -\frac{1}{b} \sum_{q=2}^n \frac{(-1)^q}{[(D_{\perp}^{q-1})^2 + (D_{\parallel}^{q-1})^2]^{\frac{1}{2}}} - \frac{1}{b} \sum_{q=2}^n \sum_{p=q}^{\infty} \frac{(-1)^{p+1}}{[(D_{\perp}^p)^2 + (D_{\parallel}^p)^2]^{\frac{1}{2}}} + \frac{(-1)^{p+1}}{[(D_{\perp}^r)^2 + (D_{\parallel}^p)^2]^{\frac{1}{2}}}, \quad (5.12)$$

where $r = |p + 2(1 - q)|$. The first term in equation 5.12 represents the interaction of an ion in chain q with the ions along a direction perpendicular to this chain (when the sheet is initially unfolded). The second and third terms represent the interactions with all other ions in the sheet.

Figure 7a shows the energies of an anion-cation chain making up part of a $(n, 0)_{sq}$ INT, as a function of the INT radius (displayed relative to the anion-cation length-scale b). As would be expected, as n increases the energy of the chain approaches the linear chain limit of $-2\ln 2/b$. The observation of a less negative energy for the chains comprising the $(n, 0)_{sq}$ INTs, compared with the linear chains (and hence the chains comprising the $(n, n)_{sq}$ INTs), is simply the result of the effective “twisting” of the chain away from linear, the effect of which becomes more pronounced as n is reduced (and the twist becomes tighter). Figure 7b shows the inter-chain energies, U^{ic} , for both the $(n, 0)_{sq}$ and $(n, n)_{sq}$ INTs. As a result, both the inter-chain interaction energies and the chain energies (figure 7) are relatively unfavorable for the $(n, 0)_{sq}$ INTs.

Figure 4 shows the results of the chain model calculations compared with the original atomistic results. The chain model successfully reproduces the trend obtained for the original atomistic calculations. Both the differences between the $(n, 0)_{sq}$ and $(n, n)_{sq}$ INT energetics, and the difference between the results obtained from the full Born-Mayer potential and the chain model, can be attributed to the relative magnitudes of the changes in

both the coulombic and short-range anion-anion interactions as the square nets are folded.

Figure 8 shows both the Born-Mayer short-range anion-cation and anion-anion interaction energies for both the $(n,0)_{sq}$ and $(n,n)_{sq}$ INTs. Although the anion-cation short-range energy dominates the anion-anion (as would be expected given the relative nearest-neighbour separations) the *change* in the anion-anion energy is much more significant for the $(n,0)_{sq}$ folding. The difference can be understood by considering the two folding chiral vectors in terms of figure 1. For the $(n,0)_{sq}$ fold pairs of nearest-neighbour anions are moved closer together whilst, for the $(n,n)_{sq}$ INTs, it is the next-nearest neighbour interactions which change most significantly.

VI. FILLING THE CARBON NANOTUBES.

The effect of the dependence of the square-net-based INTs on the direction of folding can be highlighted by performing a series of direct filling simulations as described previously [28]. For example, here we apply a model for KI shown previously to reproduce both known bulk and enclosed crystallite structures [28]. The carbon nanotubes are treated as fixed atomistic entities with the ion-carbon interactions modelled via Lennard-Jones potentials with the parameters derived by reference to the isoelectronic noble gases. A filling simulation is performed by removing a cylindrical section from an equilibrated liquid configuration (for KI evolving at $T = 900\text{K}$ compared with an estimated simulation melting point of $T_m \simeq 700\text{K}$). A fixed C-NT is placed in the cylindrical pore and the ends sealed with sections of graphene sheet or order to allow molecular dynamics to be performed in order to re-attain equilibrium. Once the system has been re-equilibrated the graphene end-groups are removed which allows the ions to enter the tube.

Figure 9 shows the filling statistics using three different sized carbon nanotubes [the $(10,10)$, $(11,11)$ and $(12,12)$ respectively]. For each C-NT six initial starting configurations are generated by extracting liquid configurations from dynamic simulations at different times such that the configurations can be considered as independent. The INT structures obtained

1 here are heavily biased towards the $(n, m)_{sq}$ where $n = m$ or $n \simeq m$, reflecting the strong
2 thermodynamic preference for these structures. These results are in contrast to the analogous
3 filling simulations in which hexagonal structures are generated, which show a full range of
4 morphologies [45].
5
6
7
8

9 VII. SUMMARY AND CONCLUSIONS.

10 In this paper we have considered the formation energetics of three basic nanotube struc-
11 tures. The carbon nanotubes and hexagonal INTs, both of whose structures can be ra-
12 tionalised in terms of folding a single sheet of percolating hexagons, when modelled with
13 relatively simple potentials, appear to show folding energies consistent with an elastic con-
14 tinuum model. As a result, these systems behave essentially as a sheet of paper in the sense
15 that the folding energies appear independent of the direction along which they are folded
16 (and hence independent of the final INT morphology). For the INT structures which can
17 be rationalised in terms of the folding of square nets, however, the folding energetics appear
18 heavily morphology dependent.
19
20
21
22
23
24
25
26
27
28
29
30
31
32

33 VIII. ACKNOWLEDGMENTS.

34 It is a pleasure to acknowledge Professor Stone's contribution to the fundamental under-
35 standing of intermolecular interactions.
36
37
38
39
40
41
42

43 IX. APPENDIX I.

44 Figure 10a shows a schematic diagram of the anions and cations in a single
45 plain perpendicular to the major INT axis for a $(n, n)_{sq}$ nanotube. Looking along
46 the major INT axis then angle between neighbouring atoms with respect to the
47 origin (the centre of the INT) is given by π/n . The distance from a given ion 0
48 to another ion labelled i in this plain, K_i , is given by
49
50
51
52
53
54
55
56
57
58
59
60

$$K_i = 2R \sin \left\{ \frac{i\pi}{2n} \right\}, \quad (9.1)$$

where R is the INT radius, defined as the distance from a point on the central INT axis vector which intersects a plain perpendicular to that vector which contains a group of ions, and an ion in this plain. The INT radius, R , can be expressed in terms of the anion-cation length-scale a as

$$R = \frac{a}{2 \sin \left\{ \frac{\pi}{2n} \right\}}. \quad (9.2)$$

As a result, the distance K_i is given by

$$K_i = \frac{a \sin \left\{ \frac{i\pi}{2n} \right\}}{\sin \left\{ \frac{\pi}{2n} \right\}} = aL_i. \quad (9.3)$$

X. APPENDIX II.

Figure 10b shows the square net sheet which can be used to construct the $(5,0)_{sq}$ INT by folding along the chiral vector, C_h . The interactions are divided into those along an anion-cation chain (intra-chain) labelled q in equation 5.12 and those between these chains (inter-chain interactions). Considering the ion coloured yellow in figure 10b, which belongs to the $q = 1$ chain, then the red and blue lines correspond to the $q = 3$ chain. The first summation in equation 5.12 represents the interaction of the ion coloured yellow with all ions along a vector perpendicular to the $q = 1$ anion-cation chain vector (*i.e.* along the yellow line in the figure). The further two summations in equation 5.12 represent the interaction of this ion with the ions to the left and right of the yellow line respectively. The figure highlights the interaction with the $q = 3$ anion-cation chain, with a number of (p, r) indices for equation 5.12 highlighted. The presence of two summations reflects the difference in anion-cation separations parallel to and perpendicular to the major axis when the sheet is folded. In the absence of this difference then the double summation can be subsumed into a single term.

Potential	ij	a_{ij}	B_{ij}	C_6
I	MX	1.50	8.68	2.09
	XX	1.50	61.66	115.987
II	MX	1.50	12.94	2.09
	XX	1.50	61.66	115.987

TABLE I. Potential parameters for the Born-Mayer potential.

System	$F/\text{eV}\text{\AA}^{-2}$
C ($n, 0$)	1.62
C (n, n)	1.57
Hexagonal INTs, potential I, ($n, 0$) _{hex}	0.73
Hexagonal INTs, potential I, (n, n) _{hex}	0.62
Hexagonal INTs, potential II, ($n, 0$) _{hex}	0.73
Hexagonal INTs, potential II, (n, n) _{hex}	0.60
Square INTs, potential I, ($n, 0$) _{sq}	1.42
Square INTs, potential II, ($n, 0$) _{sq}	1.51

TABLE II. Fit parameters assuming an R^{-2} (continuum elastic model) dependence of the folding energy.

FIG. 1. The (a) square- and (b) hexagonal-net-based INT structures constructed from the two atom unit cells highlighted in the dashed boxes and described by the unit cell vectors \mathbf{a}_1 and \mathbf{a}_2 respectively. Both sheets can be folded along a chiral vector \mathbf{C}_h to give a general $(n, m)_X$ ($X=\{\text{sq, hex}\}$) INT structure whose major axis points along the vector \mathbf{T} . The construction of the $(2, 2)_{sq}$ and $(3, 2)_{hex}$ INTs are highlighted.

FIG. 2. Energies of carbon nanotubes of morphology $(n, 0)$ (red lines) and (n, n) (black lines) as a function of their respective radii and shown relative to the energy of an infinite graphene sheet. Each successive curve shows the energy of a CNT of a given morphology as a function of the radius of that CNT. As a result, the minimum represents the relaxed radii of the fixed geometries. In addition, the energy curves for a number of alternative morphologies (green lines - the $(3, 1)$, $(3, 2)$, $(4, 1)$ and $(5, 3)$ C-NTs) are shown to highlight the absence of significant morphology-dependence in the C-NT formation energy. The inset shows the $\ln - \ln$ plot of the respective energy minima for the $(n, 0)$ and (n, n) C-NTs along with the respective linear regression fits.

FIG. 3. Energies of the hexagonal INT calculated using potential I (black lines) and potential II (red), shown relative to the energy of an infinite hexagonal net, and plotted as a function of the radii. The solid and dashed lines correspond to $(n, n)_{hex}$ and $(n, 0)_{hex}$ INTs respectively. The inset shows the corresponding $\ln - \ln$ plot of the respective energy minima along with the best polynomial fits.

FIG. 4. (a) Energies of the square-net-based INTs in the $(n, n)_{sq}$ (red lines) and $(n, 0)_{sq}$ (black lines) morphologies as a function of their respective relaxed radii and plotted relative to the energy of the respective infinite square-net sheets. The lower and upper panels show the curves calculated for potentials I and II respectively. In both panels the green and blue crosses show the results of the chain model calculations discussed in section V. In these cases the lines joining the points are shown as a guide to the eye. (b) A $\ln - \ln$ plot of the respective energy minima from both panels (potentials I and II) from part (a). The black points are for potential I and the red for potential II respectively. The \times symbols correspond to the $(n, 0)_{sq}$ INTs and the $+$ symbols to the $(n, 0)_{sq}$ INTs. The solid and dashed lines highlight the best polynomial fits.

FIG. 5. (a) $(n, n)_{sq}$ energies from the chain model discussed in section V. Key: black $+$ - both b and x fully relaxed, green $+$ - x relaxed at fixed b , \circ - both x and b fixed. Lines are drawn between the points as a guide to the eye. (b) The ratio of the length-scales a and b ($x = a/b$) as a function of the n index. The \times symbols show the calculations of Bichoutskaia and Pyper [36] for $(m \times m \times \infty)$ rocksalt crystallites. These points are plotted against the number of molecules in a plain perpendicular to the crystallite major axis. The four points at each such value represent the results of four different short-range repulsive potentials. The lines show the results from the present work. Key: black $+$ - potential I, green $+$ - potential II. The \circ symbols shows the effect of raising the short-range parameter B_{MX} to 23.0au to highlight its continued effect of increasing the effective cation radius on the geometric parameter x . Again, lines are drawn as a guide to the eye.

FIG. 6. Effective Madelung constants, $M_b(x)$, from the present work for the $(n, n)_{sq}$ INTs compared with the values from the work of Bichoutskaia and Pyper [36] on rocksalt crystallites. Key (present work): black crosses - fully relaxed x and b , Δ - b only relaxed, \circ - x only relaxed. The $+$ points shows data from reference [36] for the $(m \times m \times \infty)$ rocksalt crystallites. These data are plotted against the number of molecules in a plain perpendicular to the crystallite major axis. The dashed horizontal lines show the two dimensional plain and bulk rocksalt limits. In all cases the lines are drawn between points as a guide to the eye.

FIG. 7. The breakdown of the system energies for the $(n, n)_{sq}$ (+ and dashed lines) and $(n, 0)_{sq}$ (\times and solid lines) INTs. The upper panel (a) shows the energy of a single anion-cation chain, U_X^{chain} [$X = (n, n)_{sq}, (n, 0)_{sq}$] which is constant for the $(n, n)_{sq}$ INT. The lower panel (b) shows the inter-chain energy, U_X^{ic} . The lines are drawn between points as a guide to the eye.

FIG. 8. The short-range repulsive energies for the $(n, n)_{sq}$ (+ and green lines) and $(n, 0)_{sq}$ (\times and black lines) INTs for the anion-cation (upper panel) and anion-anion (lower panel) pairs respectively. Note the difference in y-scale in the two cases. The lines are drawn between points as a guide to the eye.

FIG. 9. Filling statistics for filling the (10,10), (11,11) and (12,12) carbon nanotubes by molten KI. Six different liquid structures are used to generate the initial configurations. The different coloured blocks indicate the final INT structure.

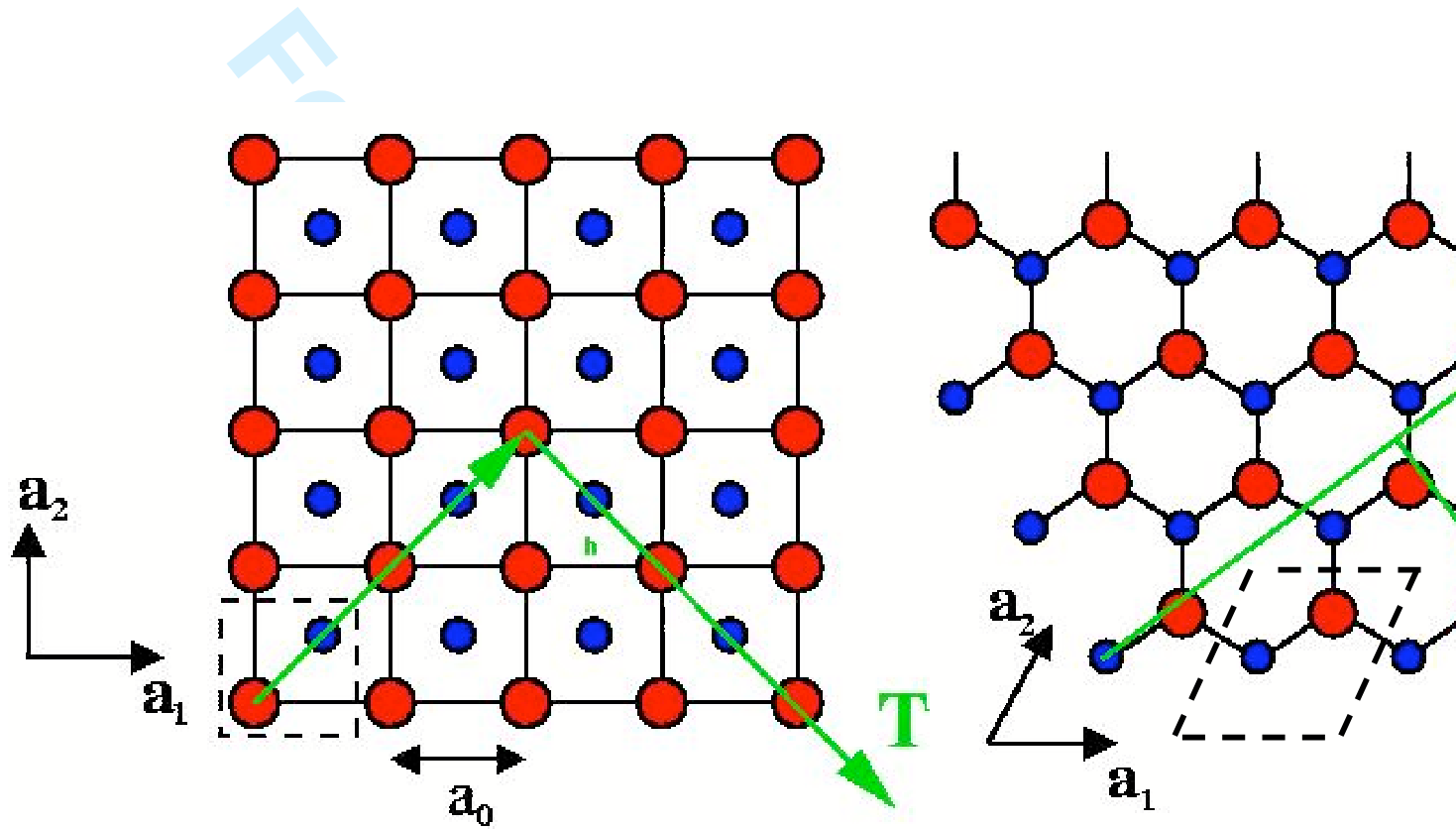
FIG. 10. (a) Schematic diagram to explain the origin of the geometric factor L_i (5.7) to account for the $(n, n)_{sq}$ nanotube folding as described in Appendix I. The red and blue circles represent the anions and cations respectively. The length-scale a is the nearest-neighbour anion-cation separation. R is the radius of the INT, defined as the distance between the origin, O (which is a point on the central axis vector which intersects with the plain of anions and cations shown) and an ion on the edge of this plain. K_i is defined as the distance from the ion labelled 0 to an ion labelled i . (b) Schematic diagram to show the formation of a $(5, 0)_{sq}$ INT from a square plain as described in Appendix II. The interaction of the ion coloured yellow (on the chain labelled by $q = 1$) can be divided into three sets of interactions. The first summation in equation 5.12 covers the interactions between this ion and the ions perpendicular to the $q = 1$ chain (*i.e.* along the yellow line. The second and third summations cover the interactions with ions to the left and right of the yellow line. For example, a number of the (p, r) indices for equation 5.12 for the interaction between the yellow ion and the $q = 3$ chain are highlighted.

- 1
2 [1] H.W.Kroto, J.R.Heath, S.C.O'Brien, R.F.Curl and R.E.Smalley (1985) *Nature*, **318**,
3 162-163.
4
5
6
7 [2] Ajayan,P.M., & Ebbesen,T.W. (1997). *Rep. Prog. Phys.* **60**, 1025-1062.
8
9
10 [3] Iijima,S. (1991). *Nature* **354**, 56-58.
11
12 [4] Bethune,D.S., Klang,C.H., de Vries,M.S., Gorman,G., Savoy,R., Vasquez,J., & Bey-
13 ers,R. (1993). *Nature* **363**, 605-607.
14
15
16
17 [5] Tenne,R., Homyonfer,M., & Feldman,Y., *Chem. Mat.*, **10**, 3225 (1998).
18
19
20 [6] Rosenfeld Hacoheh,Y., Grunbaum,E., Tenne,R., Sloan,J., & Hutchison,J.L., *Nature*,
21 **395**, 336 (1998).
22
23
24 [7] Loiseau,A., Willaime,F., Demoncey,N., Hug,G., & Pascard,H., *Phys. Rev. Lett.*, **76**, 4737
25 (1996). Suenaga,K., Colliex,C., Demoncey,N., Loiseau,A., Pascard,H., & Willaime,F.,
26 *Science*, **278**, 653 (1997).
27
28
29
30
31 [8] Armstrong,G., Armstrong,A.R., Canales,J. and Bruce P.G., *Chem. Comm.*, 2454-2456
32 (2005).
33
34
35
36 [9] C.N.R. Rao, A. Govindaraj, F.L. Deepak, N.A. Gumari, M. Nath, *Appl. Phys. Lett.*, **78**,
37 1853 (2001).
38
39
40
41 [10] M. Bar-Sadan, I. Kaplan-Ashiri, and R. Tenne, *Eur. Phys. J. Special Topics*, **149**, 71101
42 (2007).
43
44
45
46 [11] Tsang,S.C., Chen,Y.K., Harris,P.J.F., & Green,M.L.H. (1994). *Nature* **372**, 159-162.
47
48
49 [12] Sloan,J., Kirkland,A.I., Hutchison,J.L., & Green,M.L.H., *Chem. Com.* 1319 (2002).
50
51 [13] Ajayan,P.M., Ebbesen,T.W., Ichihashi,T., Iijima,S., Tanigaki,K., & Hiura,H. (1993).
52 *Nature* **362**, 522-525.
53
54
55
56
57
58
59
60

- [14] Ajayan,P.M., Ichihashi,T., & Iijima,S. (1993). *Chem. Phys. Lett.* **202**, 384-388.
- [15] Ajayan,P.M., Stephan,O., Redlich, Ph., & Colliex,C. (1995). *Nature* **375**, 564-567.
- [16] Chen,Y.K., Green,M.L.H., & Tsang,S.C. (1996). *Chem. Comm.*, 2489-2490.
- [17] Sloan,J., Cook,J., Chu,A., Zwiefka-Sibley,M., Green,M.L.H., & Hutchison,J.L. (1998). *J. Solid State Chem.* **140**, 83-90.
- [18] Sloan,J., Wright,D.M., Woo,H-G., Bailey,S.R., Brown,G., York,A.P.E., Coleman,K.S., Hutchison,J.L., & Green,M.L.H. (1999). *Chem. Comm.*, 699-700.
- [19] Sloan,J., Terrones,M., Nufer,S., Friedrichs,S., Bailey,S.R., Woo,H,-G., Rühle,M., Hutchison,J.L., & Green,M.L.H. (2002). *J. Am. Chem. Soc.* **124**, 2116-2117.
- [20] Sloan,J., Novotny,M.C., Bailey,S.R., Brown,G., Xu,C., Williams,V.C., Friedrichs,S., Flahaut,E., Callendar,R.L., York,A.P.E., Coleman,K.S., Green,M.L.H., Dunin-Borkowski,R.E., & Hutchison,J.L. (2000). *Chem. Phys. Lett.*, **329**, 61-65.
- [21] Meyer,R.R., Sloan,J., Dunin-Borkowski,R.E., Kirkland,A.I., Novotny,M.C., Bailey,S.R., Hutchison,J.L., & Green,M.L.H. (2000). *Science* **289**, 1324-1326.
- [22] Sloan,J., Grosvenor,S.J., Friedrichs,S., Kirkland,A.I., Hutchison,J.L., & Green,M.L.H. (2002). *Angew. Chem. Int. Ed.* **41**, 1156.
- [23] Philp,E., Sloan,J., Kirkland,A.I., Meyer,R.R., Friedrichs,S., Hutchison,J.L., & Green,M.L.H. (2003). *Nature (Materials)* **2**, 788-791.
- [24] Friedrichs,S., Meyer,R.R., Sloan,J., Kirkland,A.I., Hutchison,J.L., Green,M.L.H. (2001). *Chem. Commun.*, 929-930.
- [25] Lee,S.M., Lee,Y.H., Hwang,Y.G., Elsner,J., Porezag,D., & Frauenheim,T., *Phys. Rev. B*, **60**, 7788 (1999).
- [26] C  f  ,M., Cohen,M.L., & Chadi,D.J., *Phys. Rev. B*, **58**, R4277 (1998).

- [27] Seifert, G., & Hernández, E., *Chem. Phys. Lett.*, **318**, 355, 2000.
- [28] Wilson, M., & Madden, P.A., *J. Am. Chem. Soc.*, **123**, 2101, 2001.
- [29] Wilson, M., *J. Chem. Phys.*, **116**, 3027 (2002).
- [30] M. Wilson, *Chem. Phys. Lett.*, **366**, 504-509, 2002.
- [31] M. Wilson, *Nano Letters*, **4**, 299-302, 2004.
- [32] M. Wilson, *Chem. Phys. Lett.*, **397**, 340, 2004.
- [33] Wilson, M., *J. Chem. Phys.*, **124**, 124706, 2006.
- [34] Sceats, E.L., Green, J.C., and Reich, S., *Phys. Rev. B*, **73**, 125441 (2006).
- [35] R. Saito, G. Dresselhaus, M.S. Dresselhaus, *Physical Properties of Carbon Nanotubes*, Imperial College Press, (1998).
- [36] Bichoutskaia, E. and Pyper, N.C., *J. Phys. Chem. B*, **110**, 5936 (2006).
- [37] C.L. Bishop and M. Wilson, *in preparation*.
- [38] J. Tersoff, *Phys. Rev. B*, **37**, 6991 (1988).
- [39] Tibbetts, G.G., *J. Cryst. Growth*, **66**, 632 (1983).
- [40] Robertson, D.H., Brenner, D.W., & Mintmire, J.W., *Phys. Rev. B*, **45**, 12592 (1992).
- [41] Sánchez-Portal, D., Artacho, E., Soler, J.M., Rubio, A., and Ordejón, P., *Phys. Rev. B*, **59**, 12678 (1999).
- [42] Kürti, J., Zólyomi, V., Kertesz, M., and Sun, G., *New J. Phys.*, **5**, 125.1 (2003).
- [43] Ziemann, P.J. and Castleman Jr., A.W., *J. Chem. Phys.*, **94**, 718 (1991).
- [44] Wilson, M., *J. Phys. Chem.*, **B101**, 4917 (1997).
- [45] Wilson, M., *J. Chem. Soc: Faraday Trans.*, **134**, 283 (2007).

1
2
3
4
5
6
7
8
9
10
11
12
13
14
15
16
17
18
19
20
21
22
23
24
25
26
27
28
29
30
31
32
33
34
35
36
37
38
39
40
41
42
43
44
45
46
47
48
49
50
51
52
53
54
55
56
57
58
59
60



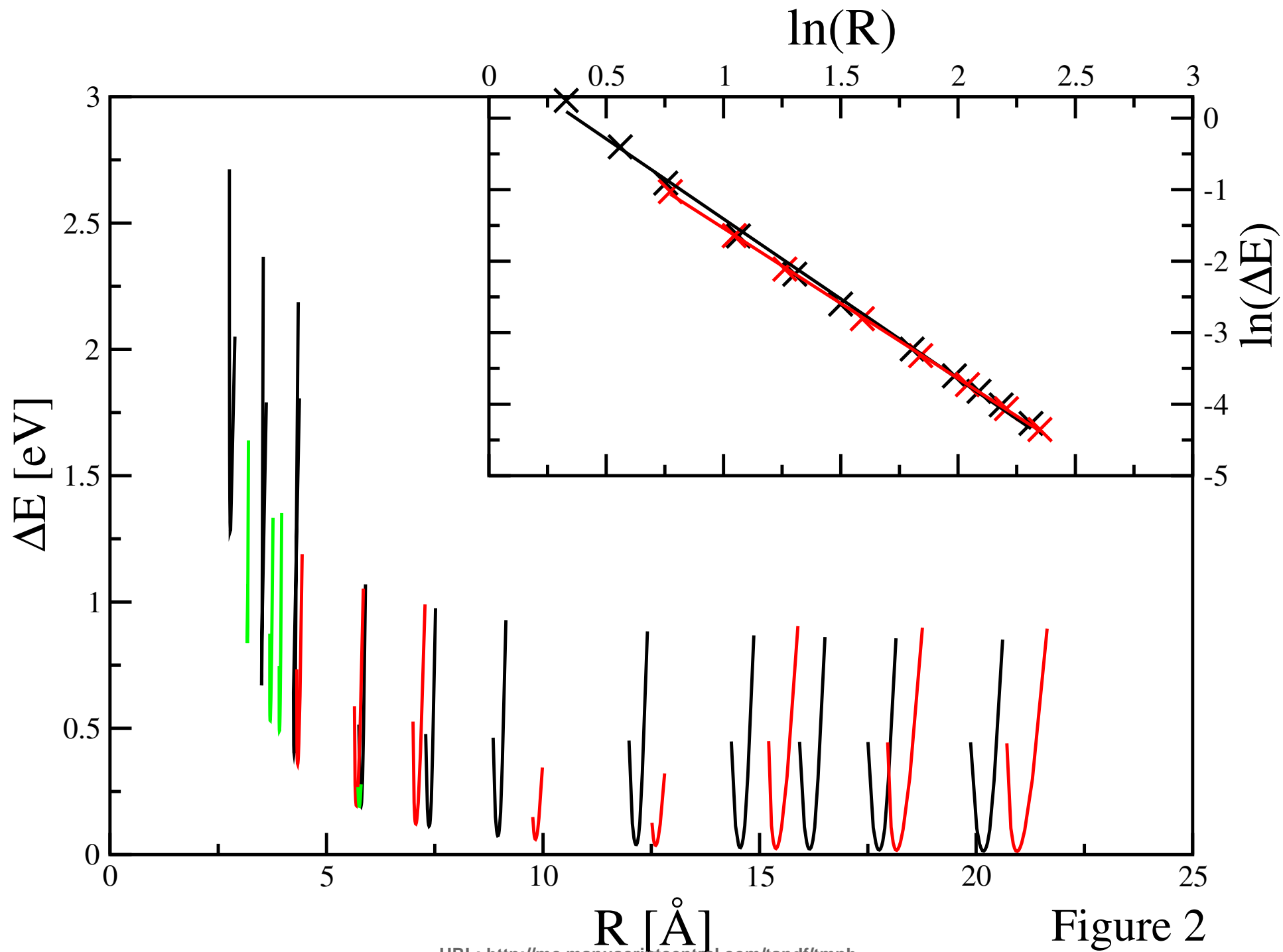


Figure 2

1
2
3
4
5
6
7
8
9
10
11
12
13
14
15
16
17
18
19
20
21
22
23
24
25
26
27
28
29
30
31
32
33
34
35
36
37
38
39
40
41
42
43
44
45
46
47
48
49

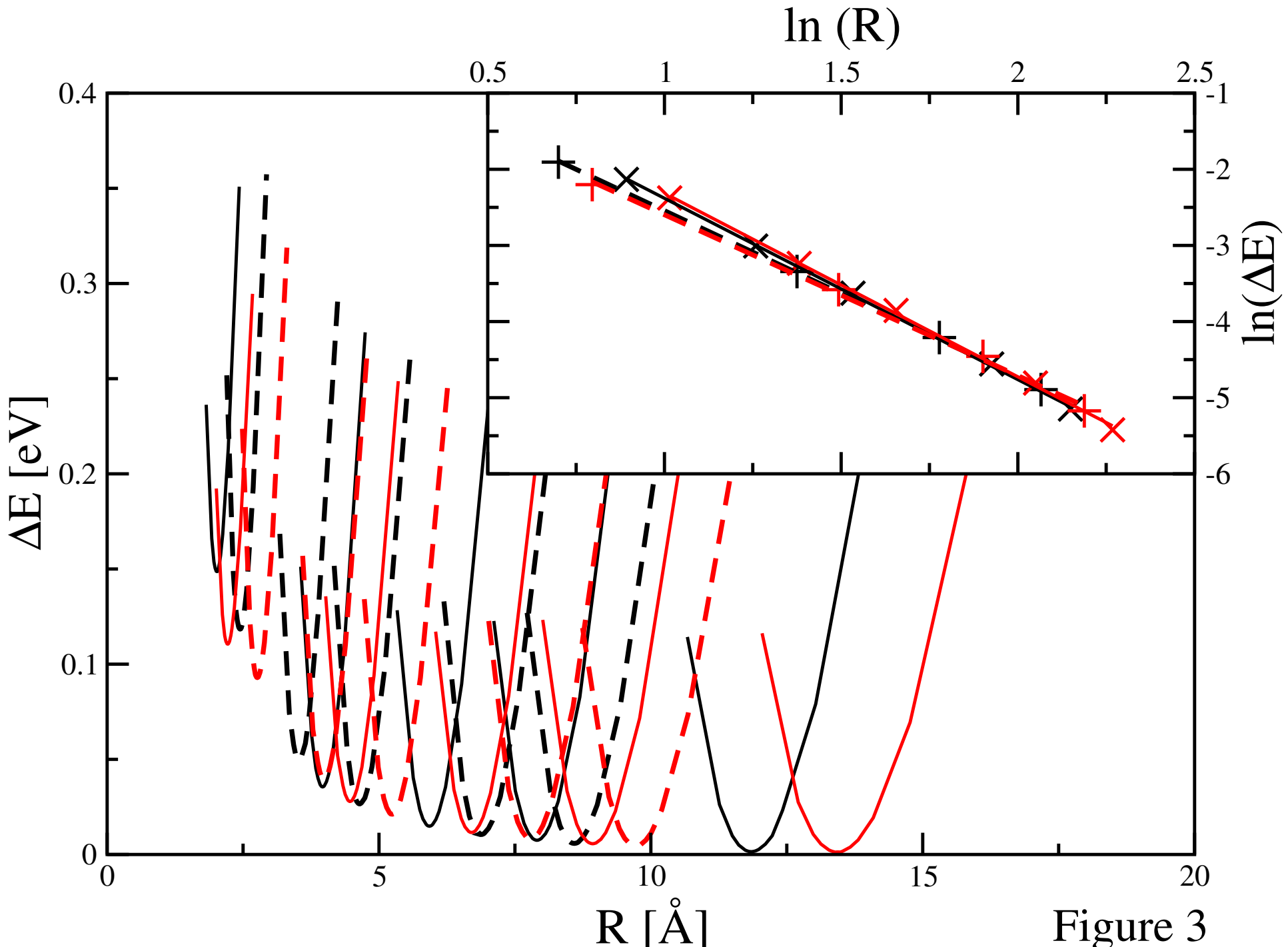
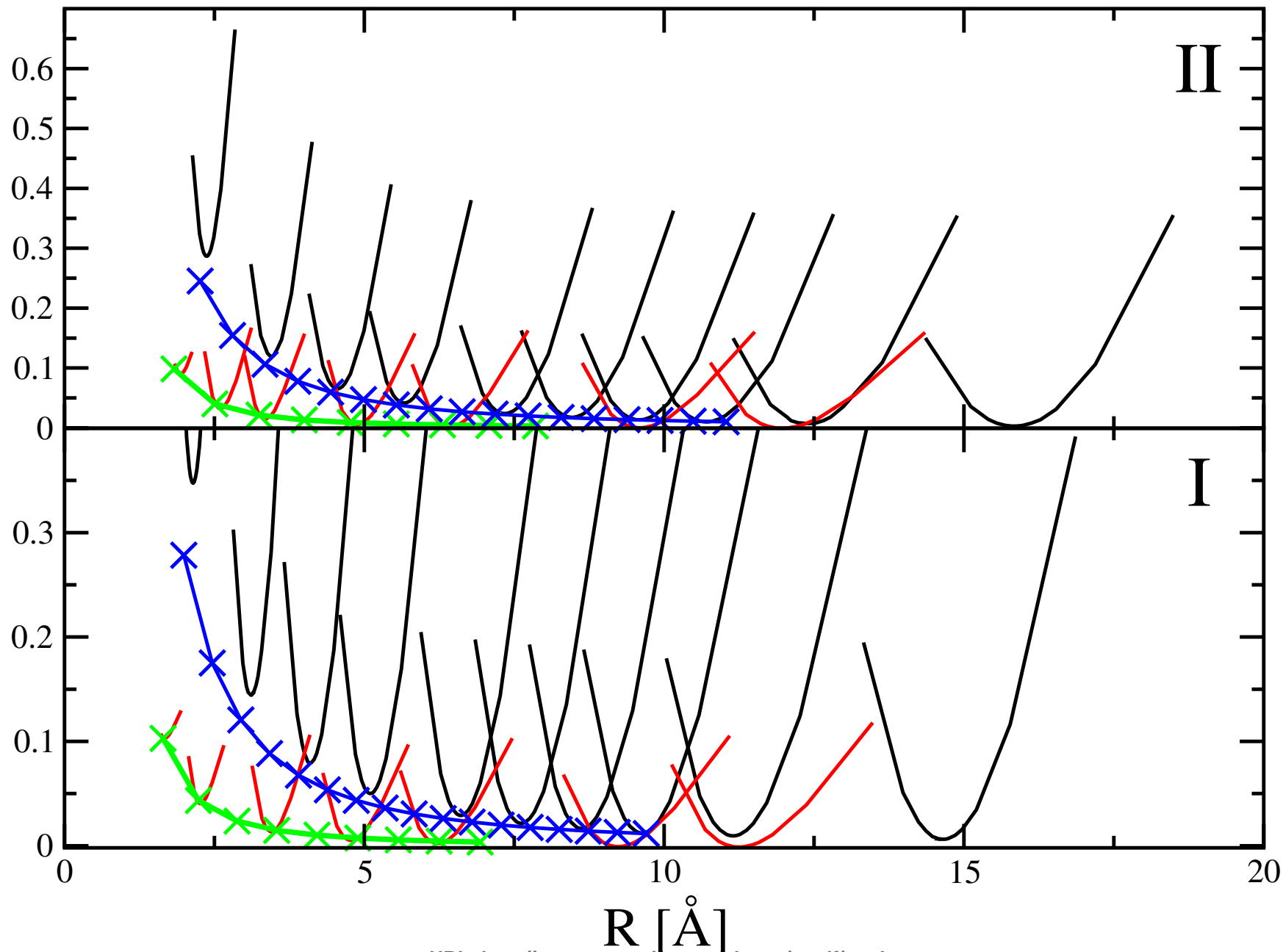


Figure 3

1
2
3
4
5
6
7
8
9
10
11
12
13
14
15
16
17
18
19
20
21
22
23
24
25
26
27
28
29
30
31
32
33
34
35
36
37
38
39
40
41
42
43
44
45
46
47
48
49

1
2
3
4
5
6
7
8
9
10
11
12
13
14
15
16
17
18
19
20
21
22
23
24
25
26
27
28
29
30
31
32
33
34
35
36
37
38
39
40
41
42
43
44
45
46
47
48
49

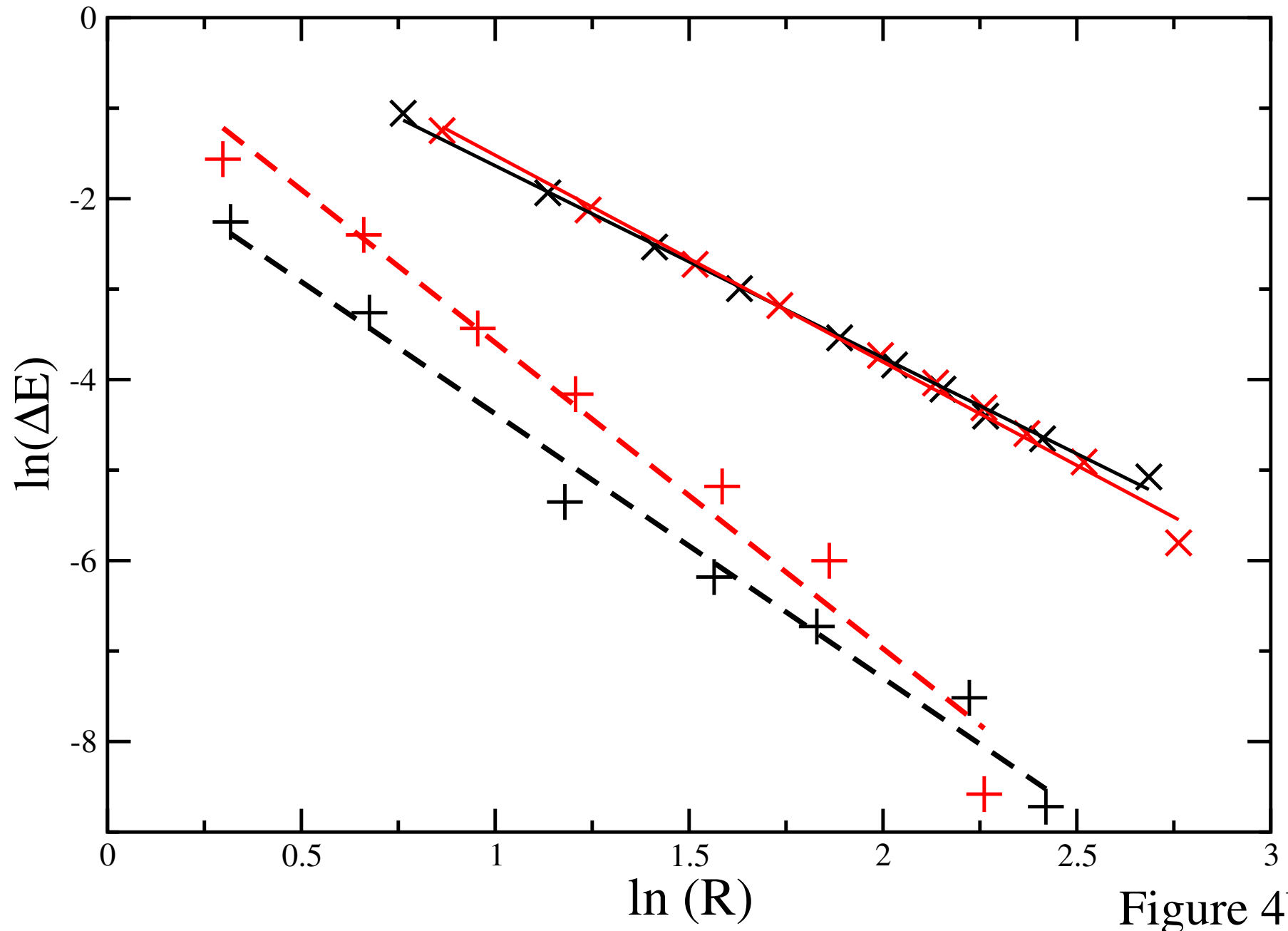


Figure 4b

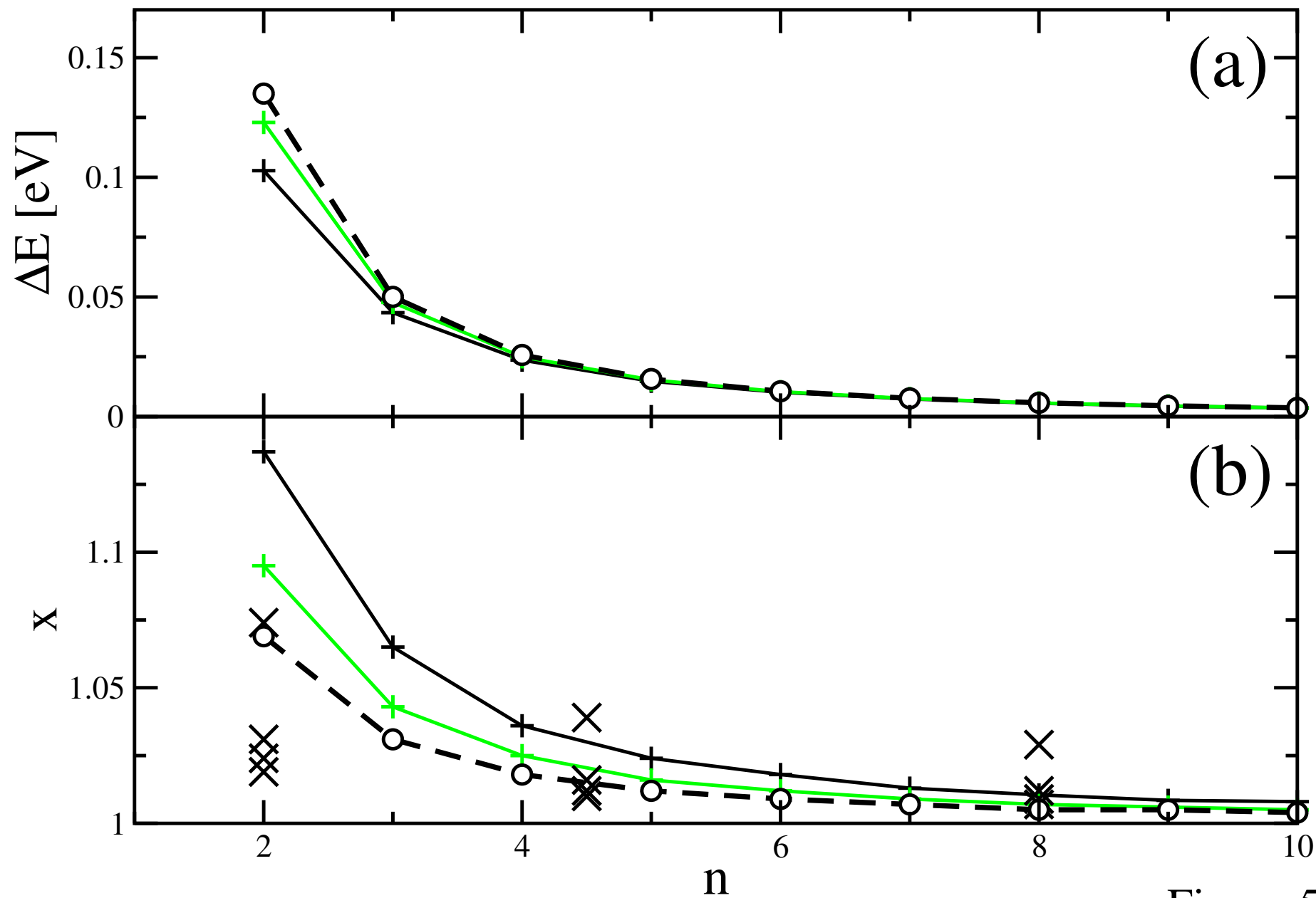


Figure 5

1
2
3
4
5
6
7
8
9
10
11
12
13
14
15
16
17
18
19
20
21
22
23
24
25
26
27
28
29
30
31
32
33
34
35
36
37
38
39
40
41
42
43
44
45
46
47
48
49

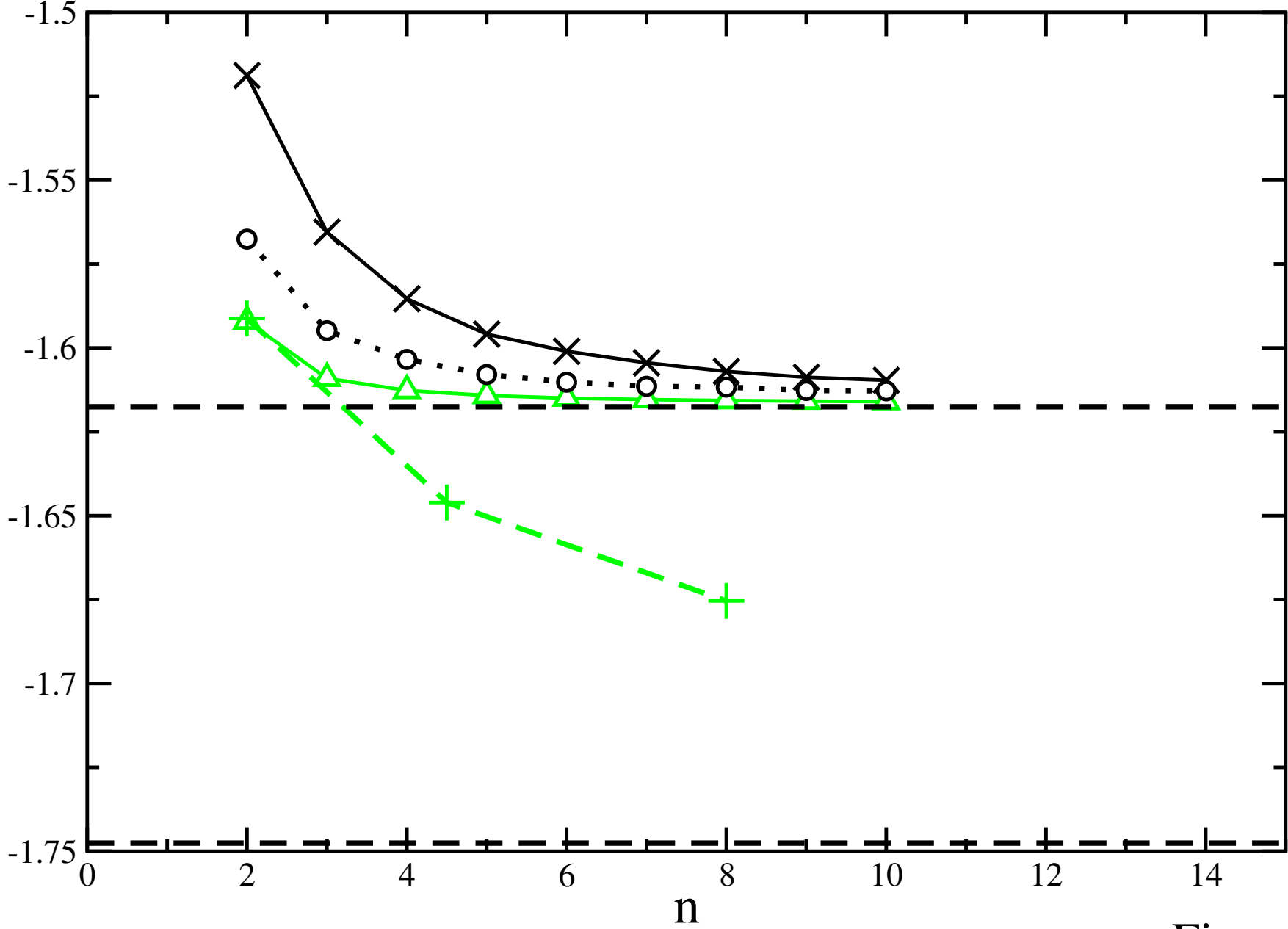


Figure 6

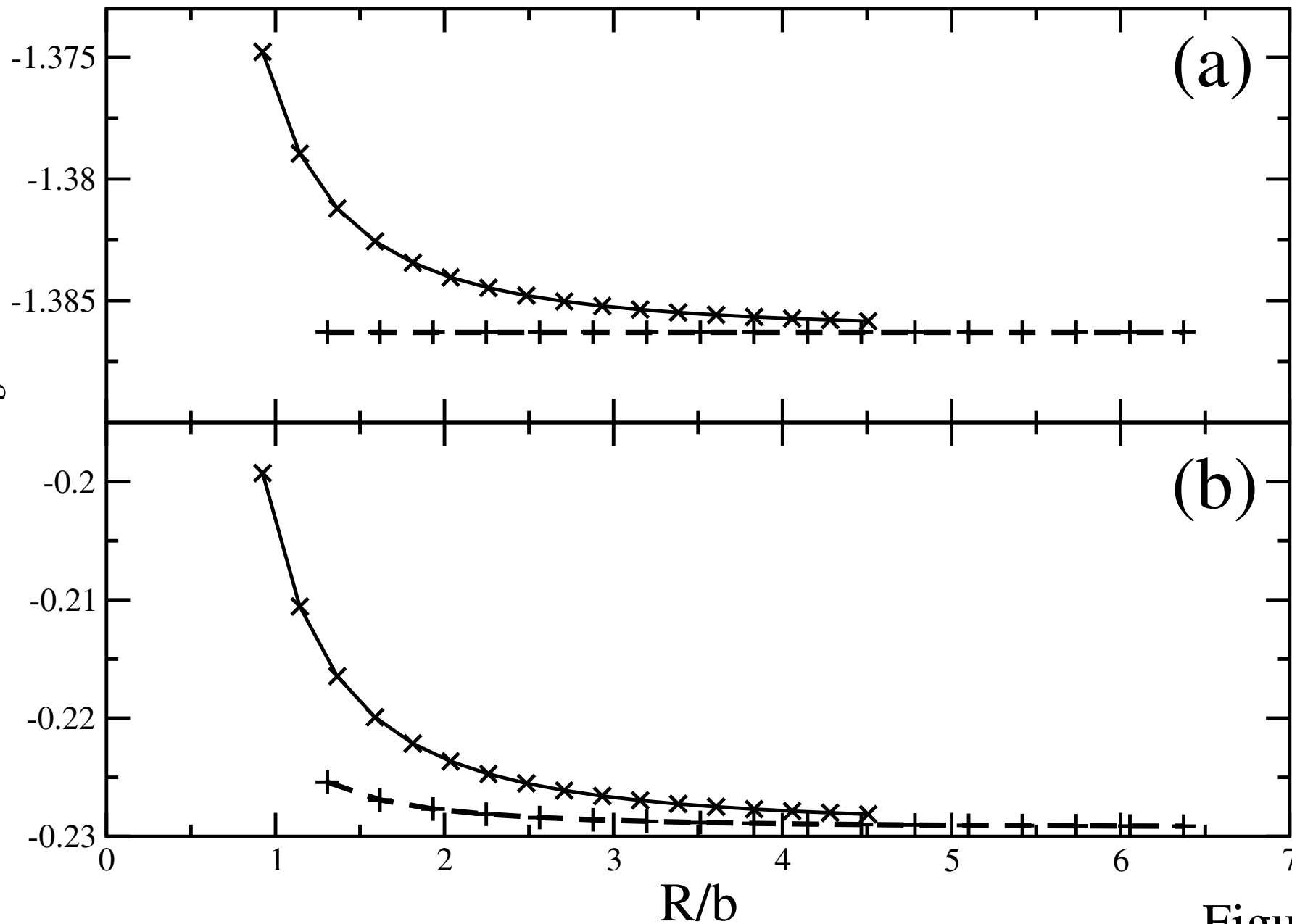
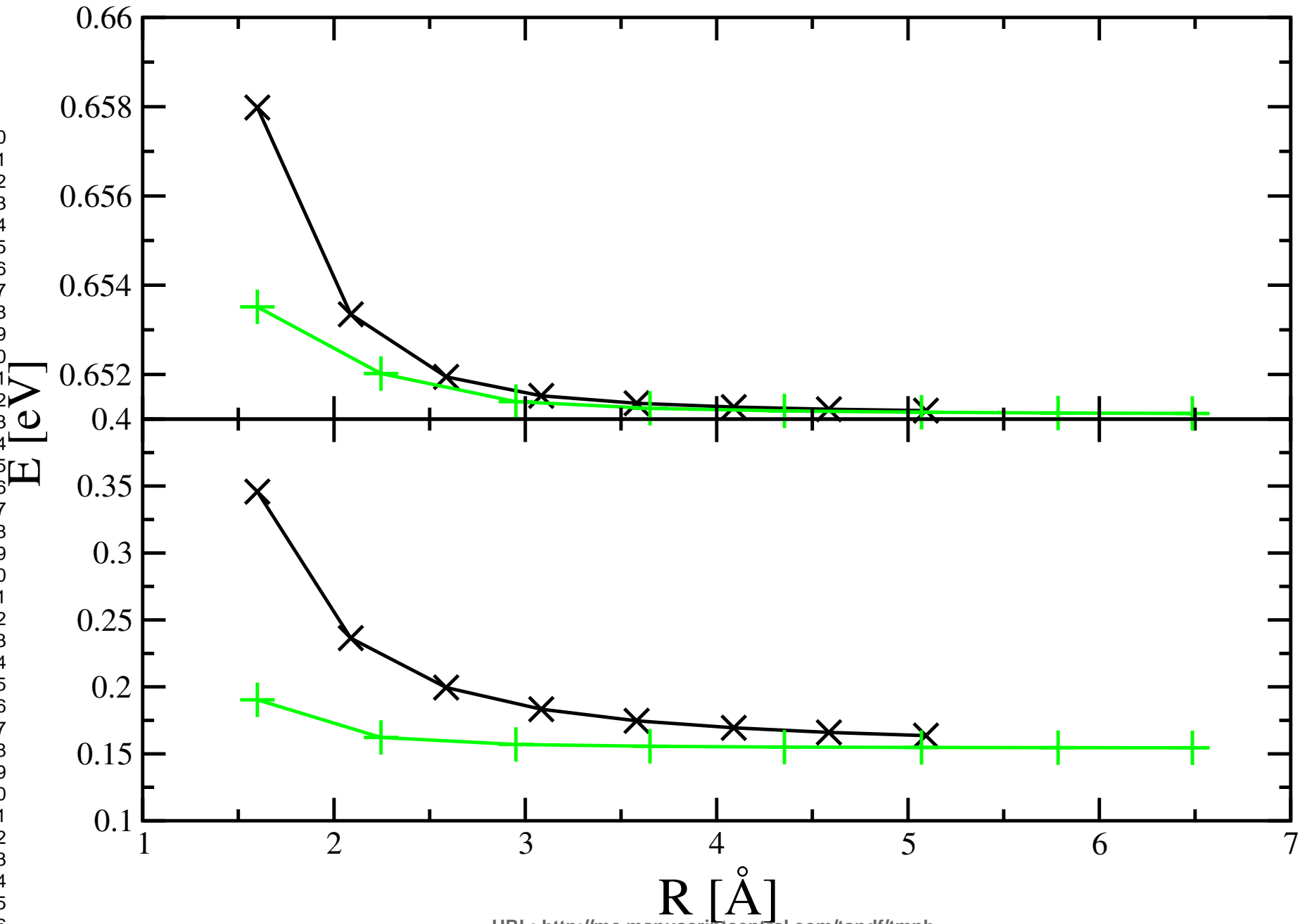


Figure 7

1
2
3
4
5
6
7
8
9
10
11
12
13
14
15
16
17
18
19
20
21
22
23
24
25
26
27
28
29
30
31
32
33
34
35
36
37
38
39
40
41
42
43
44
45
46
47
48
49



1 2 3	1	Red	Blue	Green
4 5 6	2	Blue	Green	Magenta
7 8 9	3	Red	Blue	Green
10 11 12	4	Red	Blue	Magenta
13 14 15	5	Red	Green	Magenta
16 17 18	6	Red	Blue	Magenta



(2,2)



(3,3)



(3,2)



(4,3)

1
2
3
4
5
6
7
8
9
10
11
12
13
14
15
16
17
18
19
20
21
22
23
24

URL: <http://mc.manuscriptcentral.com/tandf/tmph>


1
2
3
4
5
6
7
8
9
10
11
12
13
14
15
16
17
18
19
20
21
22
23
24
25
26
27
28
29
30
31
32
33
34
35
36
37
38
39
40
41
42
43
44
45
46
47
48
49
50
51
52
53
54
55
56
57
58
59
60

For Peer Review Only

	(10,10)	(11,11)	(12,12)
1			
2			
3			
4			
5			
6			

 (2,2)

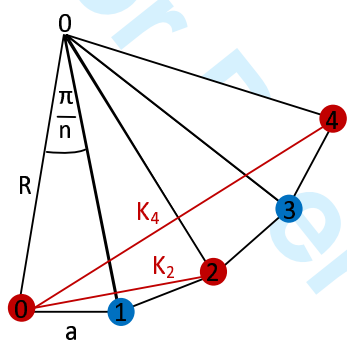
 (3,3)

 (3,2)

 (4,3)

1
2
3
4
5
6
7
8
9
10
11
12
13
14
15
16
17
18
19
20
21
22
23
24
25
26
27
28
29
30
31
32
33
34
35
36
37
38
39
40
41
42
43
44
45
46
47
48
49
50
51
52
53
54
55
56
57
58
59
60

For Peer Review Only



For Peer Review Only

